

Two-band conduction as a pathway to non-linear Hall effect and unsaturated negative magnetoresistance in the martensitic compound GdPd₂Bi

Snehashish Chatterjee, Saurav Giri, and Subham Majumdar*
*School of Physical Sciences, Indian Association for the Cultivation of Science,
2A & B Raja S. C. Mullick Road, Jadavpur, Kolkata 700032, India*

Prabir Dutta
Jawaharlal Nehru Centre for Advanced Scientific Research, Jakkur, Bangalore, 560064, India

Surasree Sadhukhan and Sudipta Kanungo†
School of Physical Sciences, Indian Institute of Technology Goa, Ponda 403401, Goa, India

Souvik Chatterjee
*UGC-DAE Consortium for Scientific Research, Kolkata Centre,
Sector III, LB-8, Salt Lake, Kolkata 700106, India*

Manju Mishra Patidar,‡ Gunadhor Singh Okram, and V. Ganesan§
UGC-DAE Consortium for Scientific Research, University Campus, Khandwa Road, Indore 452017, India

G. Das¶ and V. Rajaji
*Chemistry and Physics of Materials Unit, Jawaharlal Nehru Centre
for Advanced Scientific Research, Jakkur, Bangalore, 560 064, India*

The present work aims to address the electronic and magnetic properties of the intermetallic compound GdPd₂Bi through a comprehensive study of the structural, magnetic, electrical and thermal transport on a polycrystalline sample, followed by theoretical calculations. Our findings indicate that the magnetic ground state is antiferromagnetic in nature. Magnetotransport data present prominent hysteresis loop hinting a structural transition with further support from specific heat and thermopower measurements, but no such signature is observed in the magnetization study. Temperature dependent powder x-ray diffraction measurements confirm martensitic transition from the high-temperature (HT) cubic Heusler $L2_1$ structure to the low-temperature (LT) orthorhombic $Pmma$ structure similar to many previously reported shape memory alloys. The HT to LT phase transition is characterized by a sharp increase in resistivity associated with prominent thermal hysteresis. Further, we observe robust Bain distortion between cubic and orthorhombic lattice parameters related by $a_{orth} = \sqrt{2}a_{cub}$, $b_{orth} = a_{cub}$ and $c_{orth} = a_{cub}/\sqrt{2}$, that occurs by contraction along c -axis and elongation along a -axis respectively. The sample shows an unusual ‘non-saturating’ H^2 -dependent negative magnetoresistance for magnetic field as high as 150 kOe. In addition, non-linear field dependence of Hall resistivity is observed below about 30 K, which coincides with the sign change of the Seebeck coefficient. The electronic structure calculations confirm robust metallic states both in the LT and HT phases. It indicates complex nature of the Fermi surface along with the existence of both electron and hole charge carriers. The anomalous transport behaviors can be related to the presence of both electron and hole pockets.

I. INTRODUCTION

Heusler-based intermetallic alloys and compounds continue to be in the forefront of active research due to their multifaceted electronic and magnetic properties. They have already been identified as material for the devel-

opment of spintronics devices, magnetic actuators and switches [1–4]. So far, the major attention has been given to 3d transition metal-based Heuser compounds [5]. An early study of the rare-earth (RE) based full Heusler compounds was reported for Pd₂DySn and Pd₂HoSn, which were found to order antiferromagnetically below 5 K [6–8]. On the other hand, Pd₂RESn (RE = Tm, Lu, Y, Yb) were found to be superconducting [6]. Recently, rare-earth-bismuth-based full Heuslers and half Heuslers have attracted huge attention for their potential contribution in the field of spintronics. A number of REPdBi and REPtBi compounds were identified as topological insulators or semimetals with nontrivial band topology [9, 10]. Most importantly, REPtBi and REPdBi are identified as Weyl semimetals showing anomalous Hall effect due to

* sspsm2@iacs.res.in

† sudipta@iitgoa.ac.in

‡ Presently at Emerald Heights International School, A.B. Road, Rau, Indore 453331, India

§ Presently at Medi-Caps University, A. B. Road, Pigdamber, Rau, Indore 453331, India

¶ Presently at Elettra Sincrotrone Trieste, Strada Statale 14, km 163.5 in AREA Science Park, Basovizza, Trieste 34149, Italy

Berry curvature. [11, 12].

A close relative to the REPdBi series is the REPd_2Bi -type full Heusler compounds. However, unlike the half-Heuslers, REPd_2Bi compounds possess inversion symmetry. Most of them either order antiferromagnetically at low temperature (below 10 K) or show a nonmagnetic ground state [13, 14]. The Dy, Ho and Er compounds in the series show additional signature of the first order phase transition in the resistivity versus temperature data around 100 - 150 K [13]. For the Ho-compound, the first order phase transition is found to be associated with a structural change as evident from the appearance of additional peaks in the temperature-dependent x-ray diffraction data [14]. To the best of our knowledge, there is no report of the magnetic and transport properties of GdPd_2Bi in the literature.

Gd has total angular momentum, $J = S = 7/2$ due to the half-filled $4f$ shell, which imply that the magnetocrystalline anisotropy will be weaker. In the present work, we have performed a comprehensive study on GdPd_2Bi through our magnetic, transport and structural investigations along with density functional theory (DFT) based electronic structure calculations. Though there are several reports on the electronic structure of REPdBi and REPtBi compounds, the full Heusler based REPd_2Bi compounds are hardly investigated through *ab-initio* based electronic structure calculations. Our work identifies a martensitic type structural transition in the compound from a cubic $L2_1$ to orthorhombic $Pmma$ structure below about 150 K. The compound shows anomalous Hall coefficient and unconventional negative magnetoresistance, which can be attributed to the presence of multi-band electronic structure.

II. EXPERIMENTAL DETAILS

Polycrystalline sample of GdPd_2Bi was prepared using conventional arc melting technique and the as cast ingot was used for further measurements. The phase purity and the crystallographic structure were ensured by powder x-ray diffraction (PXRD) followed by Rietveld refinement, which was performed using MAUD program [15]. Rietveld refinement of the PXRD pattern obtained at room temperature confirms the formation of MnCu_2Al -type $L2_1$ structure (space group $Fm\bar{3}m$). The refined cubic lattice parameter is found to be $6.812(6)$ Å.

Magnetic measurements were carried out by using a commercial Quantum Design SQUID magnetometer (MPMS XL Ever Cool model). The resistivity (ρ) was measured by four probe method on a cryogen-free high magnetic field system (Cryogenic Ltd., U.K.) between 5-300 K. Thermopower measurement was performed in a lab based set up using differential technique between 10 K to 300 K. The sample was further investigated through high resolution temperature dependent x-ray diffraction (wavelength of the radiation being 0.749 Å) using synchrotron facility at the Photon Factory, National Labo-

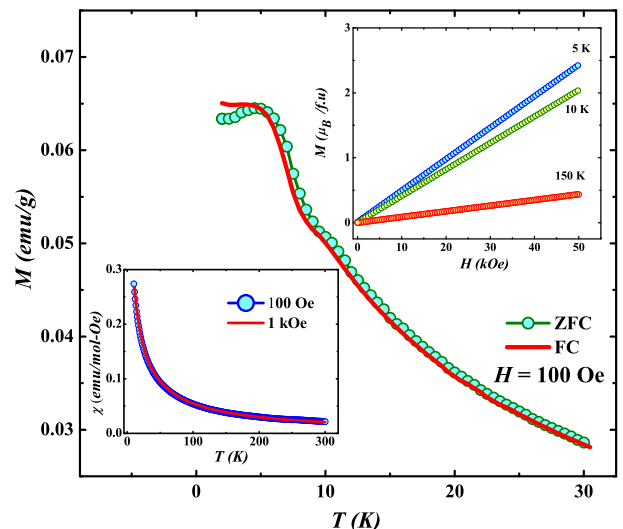


FIG. 1. M vs T curve measured at $H = 100$ Oe both in ZFC and FC protocols for GdPd_2Bi . Upper inset: isothermal magnetization data measured at different temperatures. Lower inset: magnetic susceptibility vs temperature data for $H = 100$ Oe and 1 kOe.

ratory for High Energy Physics (KEK), Japan at various sample temperatures ranging from 15 to 300 K. Heat capacity (C_P) measurement was carried out using a Quantum Design Physical Properties Measurement System.

III. THEORETICAL TECHNIQUES

DFT-based electronic structure calculations were performed using the plane-wave basis set based on a pseudo-potential framework as incorporated in the Vienna *ab-initio* simulation package (VASP) [16, 17]. The exchange-correlation functional was employed following the Perdew-Burke-Ernzerhof (PBE) prescription [18]. The effect of the spin-orbit coupling (SOC) is introduced as a full-relativistic correction term to the Hamiltonian. For the plane-wave basis, a 350 eV cut-off was applied. To take care the missing onsite Coulomb, we have used $U_{eff} = 6$ eV for the Gd, where $U_{eff} = U - J_H$, U is the onsite Coulomb interaction and J_H is the Hund's coupling term [19, 20]. The structural optimization was performed by relaxing the internal atomic positions toward the equilibrium until the Hellman-Feynman force becomes less than 0.001 eV Å⁻¹. A k-point mesh of $6 \times 6 \times 6$ in the Brillouin zone (BZ) and the electronic convergence criteria were set to be at 10^{-7} eV for self-consistent calculations.

IV. EXPERIMENTAL RESULTS

A. Magnetization

GdPd₂Bi is found to order antiferromagnetically at $T_N = 7$ K as shown in the main panel of fig 1. A weak bifurcation between field-cooled (FC) and zero-field-cooled (ZFC) magnetization (M) was observed below about 4 K. The dc magnetic susceptibility ($\chi = M/H$, H is the applied magnetic field) between 20 to 300 K can be well-fitted with the Curie-Weiss law: $\chi(T) = C/(T - \theta_P)$, where C is the Curie constant and θ_P is the paramagnetic Weiss temperature. From the good fitting of the χ vs T [not shown here], we get the effective paramagnetic moment, $\mu_{eff} = 8.0 \mu_B/f.u$ and $\theta_P = -18$ K. The half-filled $4f$ shell of the free Gd³⁺ has the effective moment $7.9 \mu_B/f.u$, which is close to the observed value. The negative value of θ_P confirms the antiferromagnetic (AFM) correlation in the system. The isothermal magnetization curves [upper inset of fig 1], measured up to $H = 70$ kOe, are found to be linear at $T = 5, 10$ and 150 K. The linear isotherm even at 5 K supports the AFM nature of the magnetic ordering.

B. Electrical Resistivity

The most fascinating observation in the present work is obtained from the transport measurement. The T -variation of ρ for GdPd₂Bi in presence of $H = 0$ and 100 kOe is presented in figs. 2 (a) and (b) respectively. The sample shows conventional decrease in ρ with temperature down to around $T = 180$ K. On further cooling, ρ follows an upturn with decreasing T down to around 30 K and eventually it shows a saturating tendency. The signature of AFM ordering is also present in the zero-field low temperature data [see the inset of fig. 2 (a)] The region of upturn shows clear thermal hysteresis indicating the transition to be first order in nature. Similar upturn was previously observed in case of other members of the family, namely HoPd₂Bi and DyPd₂Bi [13]. Since we do not observe any feature between $100 - 200$ K in the M vs T data, the observed transition is likely to be purely structural in nature.

The thermal hysteresis and the upturn survive even under an applied field of 100 kOe, and there is no significant change in the position of the upturn and the width of the thermal hysteresis. However, we observe a decrease in the value of ρ under H signifying negative magnetoresistance. Notably, a clear drop in ρ is observed below about 40 K [as evident from fig 2(b)], which indicates the emergence of a magnetic field-induced metallicity in GdPd₂Bi. The peak due to the AFM ordering in zero field [inset of fig. 2 (a)] vanishes for $H \geq 20$ kOe. Inset of fig. 2(b) shows the ρ versus T^2 plot below $T = 20$ K for different values of applied H . The system deviates completely from T^2 behaviour for $H < 20$ kOe. It is evident that $\rho(T)$ follows a T^2 dependence for $H = 100$

kOe below about 16 K, while similar T^2 variation is observed below 14 K for $H = 50$ kOe. Such T^2 variation of ρ is commonly attributed to electron-electron scattering in the Fermi liquid theory of metals. The coefficient of the T^2 term is found to be $A = 1.3 \times 10^{-8}$ and $2.4 \times 10^{-8} \Omega\text{-cm K}^{-2}$ at 100 and 50 kOe, respectively. The value of A is about one order of magnitude higher than the conventional metals such as Cu [21].

The region of upturn in the $\rho(T)$ data around 180 K is associated with the negative temperature coefficient of resistivity ($d\rho(T)/dT < 0$), and such behavior is generally observed in insulators, semiconductors or semimetals. However, the present rise can be ascribed to the structural transition, which is evident from our later analysis. It is interesting to note that similar upturn in resistivity is observed in case of several Ni-Mn-Z ($Z = \text{In, Sn, Sb}$)-based shape memory alloys around the martensitic transition [22–25].

To shed more light on the occurrence of field-induced metallicity, we have measured the field variation of ρ up to ± 150 kOe at $T = 5$ K and 10 K that eventually leads to a large negative magnetoresistance [$MR = [\rho(H) - \rho(0)]/\rho(0)$] of around -16% and -9% respectively. Hence, a conventional positive contribution from the Lorentz force can be ruled out for GdPd₂Bi. Interestingly, the negative MR in bulk GdPd₂Bi sample is ‘non-saturating’ in nature and follows the form $-\frac{\Delta\rho}{\rho} \propto H^2$ [fig. 2(c)] for H as high as 150 kOe. In addition, it is interesting to note that the negative MR persists in the compound for T as high as 120 K, which is much higher than the magnetic transition temperature ($T_N = 7$ K), although the magnitude of MR decreases with increasing T [fig. 2 (d)].

The MR can also be discussed in the framework of the semiclassical Kohler approach. In a single-band system with uniform scattering at all points on the Fermi surface, Kohler’s scaling is often found to be valid and is expressed as

$$\frac{\Delta\rho}{\rho} = f\left(\frac{\mu_0 H}{\rho}\right) \quad (1)$$

where $f(x)$ is a temperature-independent implicit function [26]. $\Delta\rho/\rho$ versus H/ρ measured at different temperatures should fall into a single curve. However, deviation from the general Kohler plot can be attributed to the reconstruction of Fermi surface for nesting and/or to the existence of multi-carrier electronic transport [27–29]. Interestingly the title compound is found to violate the Kohler’s rule (not shown here) which might be due to the existence of two type of carriers.

C. Heat capacity

Fig. 3(a) presents the low temperature $C_p(T)$ data measured in zero magnetic field as well as under $H = 60$ kOe. The zero-field data show a clear λ -like anomaly

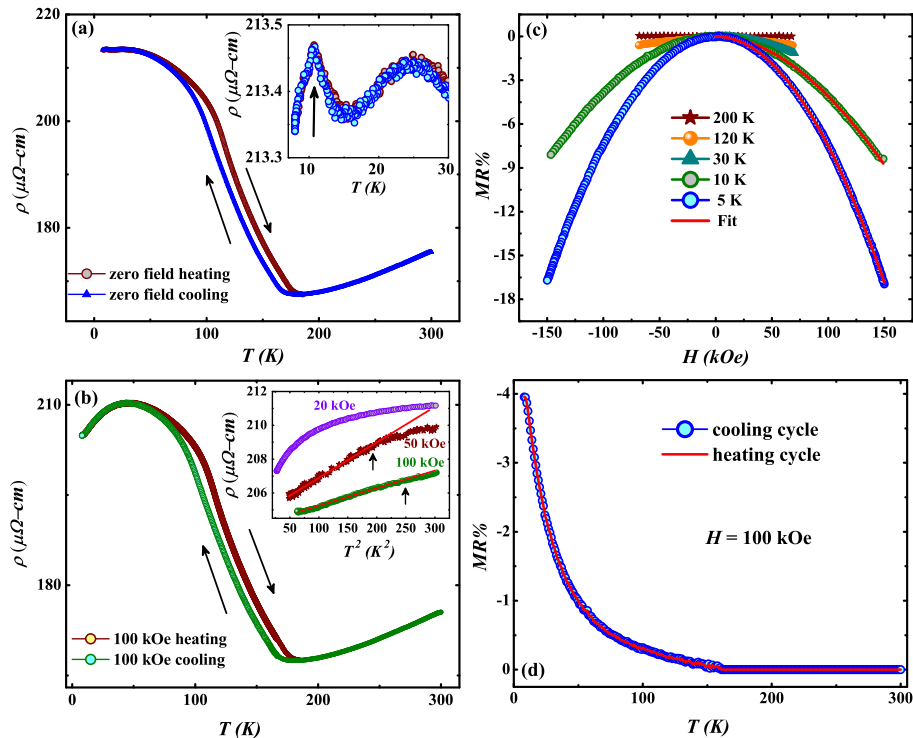


FIG. 2. The electrical resistivity as a function of temperature at (a) $H = 0$ kOe and (b) 100 kOe for GdPd₂Bi. Insets: (a) the enlarged view of the low- T region of $\rho(T)$ measured at $H = 0$ kOe and (b) the T^2 behaviour of the low- T regime at different H . (c) the magnetoresistance as a function of applied magnetic field measured at different constant temperatures. The red line is the H^2 fit to the magnetoresistance data. (d) The magnetoresistance as a function of temperature measured at $H = 100$ kOe.

around 9.5 K, which matches well with the AFM transition observed in the magnetization data. Under the application of 60 kOe magnetic field, the transition does not get suppressed, albeit the peak slightly shifts towards lower T (8.5 K). We have also calculated the change in entropy (ΔS) due to the application of H (magneto-caloric effect) [30] around T_N using the following relation.

$$\Delta S(T) = \int_0^T [C_p(H)/T - C_p(0)/T] dT. \quad (2)$$

$\Delta S(T)$ is found to be negative with a sharp anomaly at the magnetic transition temperature [inset of fig. 3(a)]. ΔS attains a moderate value of 2 J/kg-K at T_N , which is connected to the field induced shift of T_N to lower T .

At high temperature, C_p vs T data shows a peak around $T_p = 162$ K for both 0 kOe and 60 kOe measurements [fig. 3(b)]. The peak in C_p occurs around the temperature where the upturn in the $\rho(T)$ data is observed. Such feature is associated with the structural phase transformation as mentioned in section F. The C_p data around T_p do not show any change due to the application of H . Interestingly, the heating and the cooling data show thermal hysteresis around this structural transition, which mimics the similar observation in the $\rho(T)$ measurements. The C_p value at 300 K is found to be pretty close to the value obtained by using the Dulong-Petit method ($= 3pR$, where R is the universal gas con-

stant and p ($= 4$ here) is the number of atoms per formula unit) for the sample (~ 100 J/mol-K).

D. Thermopower

We have performed the thermopower measurement in terms of Seebeck coefficient (α_S) [31] in zero field as shown in fig. 4. GdPd₂Bi shows negative value of α_S between 25 - 270 K attaining a maximum value with magnitude ~ 3 μ V/K. $\alpha_S(T)$ shows a hump-like feature around 140 K, which matches well with the feature observed in the $\rho(T)$ data. Interestingly, α_S changes its sign and turns positive below 25 K and attains a value of ~ 1 μ V/K at 12 K, which may be due to the presence of both electrons and holes in the system. In a two-carrier system the thermopower is often expressed as

$$\alpha_S = \frac{\sigma_h \alpha_{S,h} + \sigma_e \alpha_{S,e}}{\sigma_h + \sigma_e} \quad (3)$$

where σ is the electrical conductivity and the subscripts h and e denotes the hole and electron contributions, respectively. Thus, eqn 3 makes it clear that, $\alpha_S(T)$ might exhibit change in sign with temperature in the case of a two carrier system [28]. Notably, we find that GdPd₂Bi is the only compound in the REPd₂Bi series which predominantly shows negative value of α_S [13]. On the other

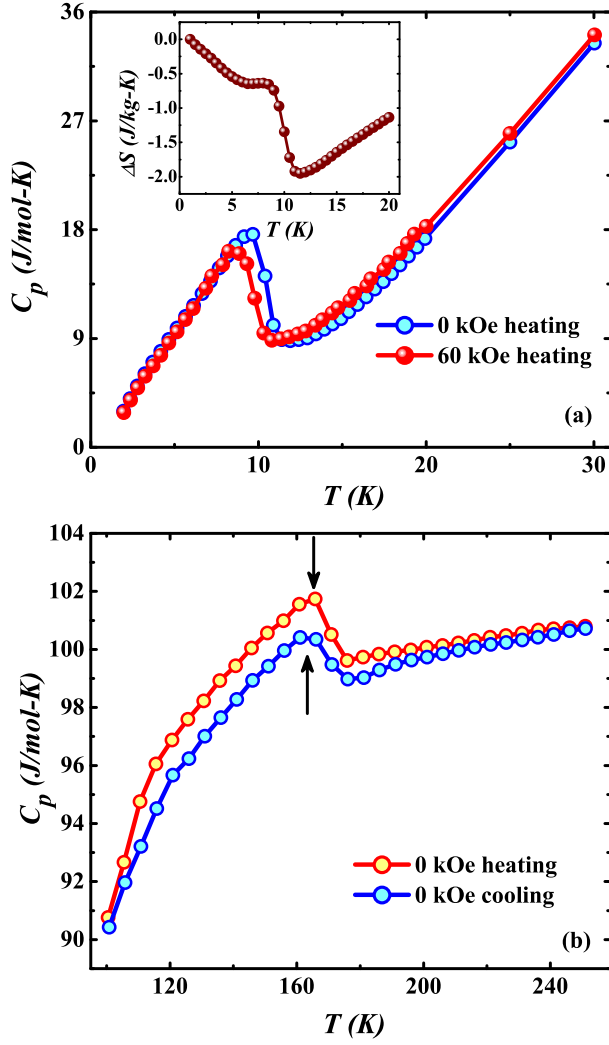


FIG. 3. (a) Heat capacity (C_p) as a function of temperature in the range (a) 2 K-30 K and (b) 100 K-200 K measured under 0 kOe and 60 kOe for GdPd₂Bi. Inset of (a) shows ΔS versus T plot.

hand, REPd₂Sb compounds show negative α_S value but they do not undergo any structural transition (lack of thermal hysteresis) [13, 32]. Bi-based compounds are often found to be potential candidates for thermoelectric applications [33]. But in case of GdPd₂Bi, the power factor (PF) is rather low ($\sim 25 \mu\text{W m}^{-1}\text{K}^{-2}$).

E. Hall measurements

The Hall resistivity (ρ_{xy}) for GdPd₂Bi was determined as the antisymmetric part of the measured transverse voltage, $\rho_{xy} = t[V_{xy}(+H) - V_{xy}(-H)]/2I$, where t is the thickness of the sample, I is the applied current and V_{xy} is the transverse voltage generated. Variation of ρ_{xy} with H measured at different constant temperatures up to $H = 70$ kOe is depicted in fig. 5(a) [40, 41]. The nega-

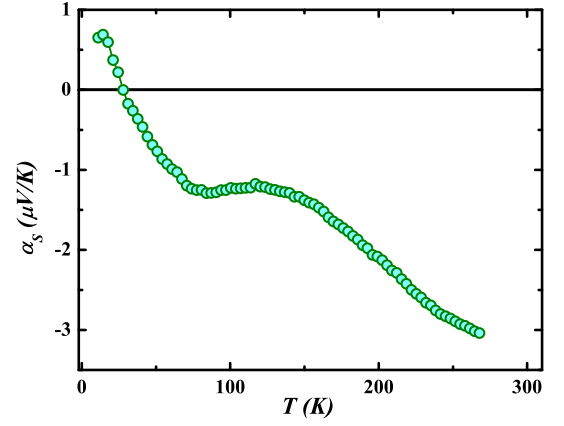


FIG. 4. Seebeck coefficient as a function of temperature for GdPd₂Bi.

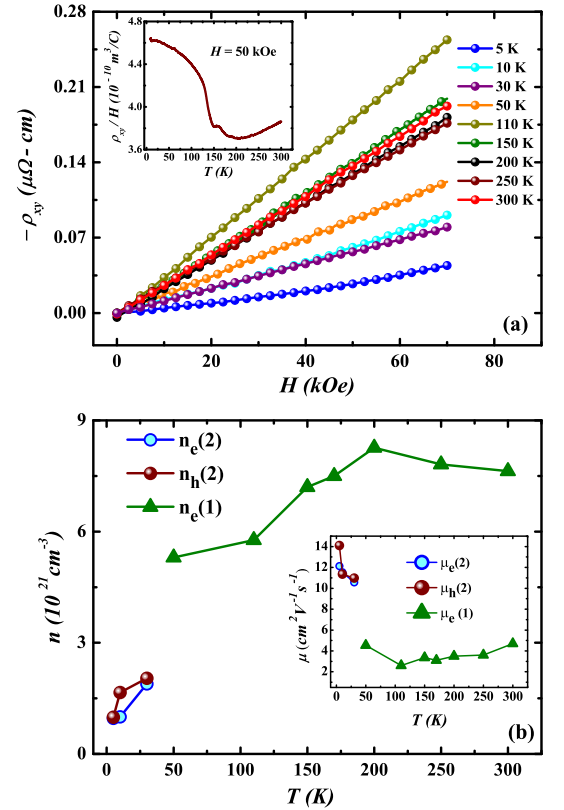


FIG. 5. (a) ρ_{xy} vs H at different constant temperatures. Inset shows T variation of ρ_{xy}/H for $H = 50$ kOe. (b) T -variation of carrier concentration. Inset: T variation of Hall mobility for GdPd₂Bi. $n_{e,h}(i)$ and $\mu_{e,h}(i)$ denote carrier concentration and carrier mobility obtained from single carrier ($i = 1$) and two carrier ($i = 2$) model, respectively.

tive value of ρ_{xy} at all measured temperatures indicates electron to be the majority carrier in the system. As temperature is lowered from room temperature, ρ_{xy} vs H show linear variation above about 30 K. However, on further lowering of T , ρ_{xy} turns non-linear for $T \leq 30$ K suggesting that a simple picture of the single-carrier

model for the conventional Hall effect is inadequate for the sample, at least below 30 K.

We have depicted the T -variation of ρ_{xy}/H in the inset of fig. 5(a), and it is strongly T -dependent along with a clear anomaly around the temperature of thermal hysteresis observed in the $\rho(T)$ data.

As mentioned earlier, the Hall resistivity at low- T ($T = 5$ K, 10 K and 30 K) shows a non-linear nature and follows a concave upward shape as can be seen from the fig 6. The non-linearity at low- T may arise either due to the presence of more than one charge carrier or due to the anomalous Hall contribution [42]. Since the sample shows a perfect linear variation of M with H [see upper inset of fig. 1], the nonlinearity of the $\rho_{xy}(H)$ cannot be simply attributed to the anomalous Hall effect (AHE) of magnetic origin. Notably, α_S turns from negative to positive below about 25 K. Such behavior may be due to the presence of both electrons and holes in the system. Therefore, a multiband model consisting of holes and electrons seems logical to describe the nonlinearity in ρ_{xy} .

We invoked the following two carrier model to fit the Hall resistivity [43]:

$$\rho_{xy}(H) = \frac{H}{e} \left[\frac{(n_h \mu_h^2 - n_e \mu_e^2) + (n_h - n_e)(\mu_h^2 \mu_e^2) H^2}{(n_h \mu_h + n_e \mu_e)^2 + (n_h - n_e)^2 \mu_h^2 \mu_e^2 H^2} \right] \quad (4)$$

Here n_h , n_e , μ_h and μ_e are the carrier density and mobility of hole(h) and electron(e) respectively. As can be seen from fig. 6, ρ_{xy} for $T = 5, 10$ and 30 K can be fitted with eqn. 4 suggesting that the two carrier model can successfully describe the experimentally measured data below about 30 K. However, the linear nature of ρ_{xy} versus H above 30 K prompted us to express the Hall resistivity data via an effective single-carrier model, where the normal Hall-coefficient ($R_H = \rho_{xy}(H)/H$) is calculated from the slope of high-field ($40 \text{ kOe} < H < 70 \text{ kOe}$) data. Hence, ρ_{xy} is fitted with two different models for $T < 30$ K regime and $T > 30$ K temperature range, where two-carrier and single-carrier models respectively, gives best fit of the experimental data [44, 45].

The temperature dependence of the carrier concentration (n_e and n_h) and Hall mobility (μ_e and μ_h) are shown in fig. 5(b). The extracted value of electron carrier concentration increases from $9.6 \times 10^{20} \text{ cm}^{-3}$ at 5 K (derived from two carrier model) to $7 \times 10^{21} \text{ cm}^{-3}$ (obtained from single carrier model, $n_e = \frac{1}{R_H e}$) at room temperature for GdPd₂Bi which is in line with the typical of semimetallic materials [46, 47]. The Hall mobility (μ) is also deduced from the linear fitting of the ρ_{xy} data using the equation: $\mu = R_H/\rho(H = 0)$. μ decreases with increase in T and then saturates at higher temperatures above about 110 K [see inset of fig 5(b)]. With lowering of T , n_e increases slightly down to 200 K and then decreases sharply, around the temperature range where the thermal hysteresis is observed. Thereafter, it continues to decrease down to 5 K.

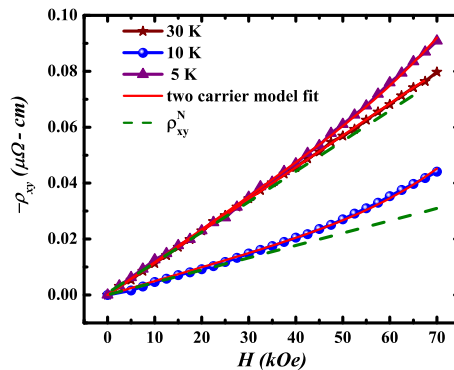


FIG. 6. ρ_{xy} vs H for $T = 5, 10$ and 30 K along with the fit of two carrier model (eqn 4). ρ_{xy}^N denotes the linear Normal Hall contribution.

F. Temperature evolution of structural parameters

Synchrotron diffraction performed at different constant temperatures are plotted in fig. 7(a). It shows [see figs. 7(a) and (b)] the change in the pattern as T is lowered from 300 K to 15 K. To highlight the change, the temperature evolution of the most intense (220) peak of the cubic phase is shown in fig. 7(b). Splitting of the main peak with the decrease in T is consistent with the loss of cubic symmetry, and the structure presumably attains a lower symmetry. Earlier Gofryk *et. al.* proposed the existence of a structural transition in the REPd₂Bi series of compounds [13], and the low- T crystal structure was reported to be orthorhombic ($Pnma$) [14].

We have carefully analyzed the data using Rietveld refinement technique and the fitted data for the representative temperature 15 K are shown in fig. 7(c). We used ISODISTORT [48, 49] software to identify all the possible list of non-cubic, non-isomorphic subgroups of the parent cubic structure. We find that the orthorhombic $Pnma$ generates all the experimentally observed reflections correctly and converge well with the data. In the intermediate temperatures, both cubic and orthorhombic structures co-exist and we have considered both the phases to refine the diffraction data. The thermal evolution of the lattice parameters is plotted (with respect to the cubic lattice parameter, a_{cub}) in fig. 8(a). The refined lattice parameters for the cubic (at 300 K) and orthorhombic (at 15 K) phases are found to be $a_{cub} = 6.812(6) \text{ \AA}$ and $a_{orth} = 9.766(1) \text{ \AA}$, $b_{orth} = 6.582(5) \text{ \AA}$ and $c_{orth} = 4.824(1) \text{ \AA}$ respectively. In case of a cubic to orthorhombic structural phase transition, the lattice parameters for the low-temperature (LT) orthorhombic unit cell is associated to the high-temperature (HT) cubic structure by the relation: $a_{orth} = \sqrt{2}a_{cub}$, $b_{orth} = a_{cub}$ and $c_{orth} = \sqrt{2}a_{cub}$ [50]. The c/a ratio turns out to be close to 0.75 indicating considerable distortion of the cubic cell as temperature is lowered. The cell volume around the thermal hysteresis regime changes around 2% between the low- and high-temperature phases which is similar to the cell

volume change of the ferromagnetic shape memory alloy, Ni₂MnGa [50]. The atomic positions for the cubic and orthorhombic structures are given in table I. These values are similar to those of other Heusler-based shape memory alloys, such as Co₂NbSn [51] and Ni_{2.04}Mn_{1.4}Sn_{0.56} [52], undergoing martensitic type phase transition.

For the 15 K data, there is a finite percentage of cubic phase present suggesting the co-existence of both the phases even at low- T region. The variation of phase fraction consisting of the orthorhombic phase and cubic phase with temperature is presented in fig. 8(b). Increase in the fraction of orthorhombic phase along with the decrease of cubic phase with decrease in temperature can be clearly observed. This observation supports the occurrence of phase transformation, as also evident from the thermal hysteresis in the ρ vs T data along with the anomaly in the high temperature C_P data.

V. THEORETICAL RESULTS

A. Density of states

The first principles electronic structure calculations have been done for both LT and HT phases of GdPd₂Bi. The calculated spin polarized GGA+ U_{eff} density of states (DOS) are shown in fig. 9(a) and fig. 9(b) for high and low temperature phases of GdPd₂Bi respectively. From the DOS, it is clear that both the high and low temperature phases are metallic in nature with small but finite DOS contributions at the Fermi energy in the both spin channels. The calculated spin magnetic moments at the position of Gd ions/site is $\approx 7.10 \mu_B$ /site for both high temperature cubic and low temperature orthorhombic structures. Whereas, the induced magnetic moment at the Pd and Bi is very small around $-0.03 \mu_B$. Point to be noted that, the induced moment at the Pd and Bi sites are of opposite sign to that of the sign of the Gd magnetic moment. The electronic structures of both low and high temperature phases have been verified by varying the onsite Coulomb correlations i.e. U_{eff} from 0 to 6 eV at the rare-earth element Gd site. As the onsite coulomb correlation increases, the Gd- $4f$ states are moving apart as shown clearly in fig. 9, without opening any gap at the Fermi energy, confirming the robustness of the metallic nature of the electronic structure.

B. Magnetic configuration

Experimentally, it has been found that the antiferromagnetic correlation for both high and low temperature. Therefore, it is pertinent to calculate the total energies of different spin configurations for both HT and LT structures. The calculated energetics are shown in table II. The results show that in both the structures the AFM configuration is energetically lower than the ferromagnetic configuration by 3.77 (2.95) meV/f.u. for HT (LT)

structures (as mentioned in table 2). We have calculated various other spin configurations as well. However, the presented spin configurations in fig. 10 are energetically lower than the other antiferromagnetic configurations. In the HT cubic structure, the Gd only sublattice as shown in the fig. 10(a) forms a regular tetrahedral unit with $\uparrow\downarrow\uparrow\downarrow$ spin arrangement. On the contrary, in the case of LT orthorhombic structure, due to reduction of the symmetry, the Gd atoms form an isosceles triangle with antiferromagnetic arrangement. As a whole, the spins on the Gd atoms are arranged parallel in the bc plane and coupled anti parallel along the crystallographic a direction.

C. Band structure

The robustness of the metallicity and the electronic structure has been also analysed in the presence of the spin-orbit coupling for both HT and LT phases. The fig. 11 shows the band structure in presence of the Coulomb correlation U and the SOC in the AFM ground state spin configurations. From the band structure it is very clear that even in the presence of the SOC and AFM correlation, the metallicity is preserved. Moreover, careful investigation reveals that for both the HT (fig. 11(a)) and LT (fig. 11(b)) configurations, the valence and conduction bands cross the Fermi energy. For example, in the HT cubic phase, the valence bands cross the Fermi energy in the $X-U$ direction of the BZ, whereas the conduction bands in multiple region such as $K-\Gamma-L$ and $\Gamma-X$ in the BZ. Similarly, for the LT phases, the conduction bands cross the E_F about the Γ , Z and Y points in the BZ. However, the valence bands cross the E_F along the $X-\Gamma-Z$, $U-Y$ and $S-T$ directions in the BZ. The bands that cross the Fermi energy dominantly contribute from the Pd- $4d$ and Bi- $5p$ orbitals. The effect of SOC on the magnetic moment is minimal, except that there is small orbital magnetic moment at the Gd site of the order of $0.02 \mu_B$.

D. Fermi surface

We have plotted the band width crossing the E_F , and the corresponding Fermi surfaces in presence of the SOC for both HT and LT phases in fig. 12(a) and (b), respectively. From the band widths, it is clear that both electron pockets and hole pockets are present in both HT and LT phases of the title compound. However, careful investigation of the fig. 11 and 12, confirms that the hole pocket is more dominant in the LT phase than the HT phase. In fig. 12(a), the bands crossing the Fermi energy and forming electron pockets are predominant in nature. The corresponding Fermi surfaces are also shown in the inset of fig. 12. From fig. 12(a) insets, it is clear that the electron pocket Fermi surfaces are mainly three types, whereas- the hole pocket Fermi surfaces are of one type,

TABLE I. Crystallographic parameter of the sample as obtained from the refinement of the PXRD data.

Temperature (K)	300					15				
Structure/space group	$L2_1$ cubic $Fm\bar{3}m$					Orthorhombic $Pmma$				
Cell parameters	$a_{cub} = 6.812(6)$ Å					$a_{orth} = 9.766(1)$ $b_{orth} = 6.582(5)$ $c_{orth} = 4.824(1)$ Å				
Cell volume (Å ³)	316.24(1)					309.63(5)				
Standard deviation (σ_D)	1.77					1.56				
Atoms	Site	x	y	z	B_{iso}	Site	x	y	z	B_{iso}
Gd	4b	$\frac{1}{2}$	$\frac{1}{2}$	$\frac{1}{2}$	0.5(3)	2a	0	0	0	1.1(2)
						2f	$\frac{1}{4}$	$\frac{1}{2}$	0.509(1)	0.9(1)
Pd	8c	$\frac{1}{4}$	$\frac{1}{4}$	$\frac{1}{4}$	0.4(4)	4h	0	0.266(5)	$\frac{1}{2}$	0.7(1)
						4k	$\frac{1}{4}$	0.265(2)	0.031(9)	0.45(9)
Bi	4a	0	0	0	1.1(9)	2b	0	$\frac{1}{2}$	0	1.2(1)
						2e	$\frac{1}{4}$	0	0.503(3)	1.1(5)

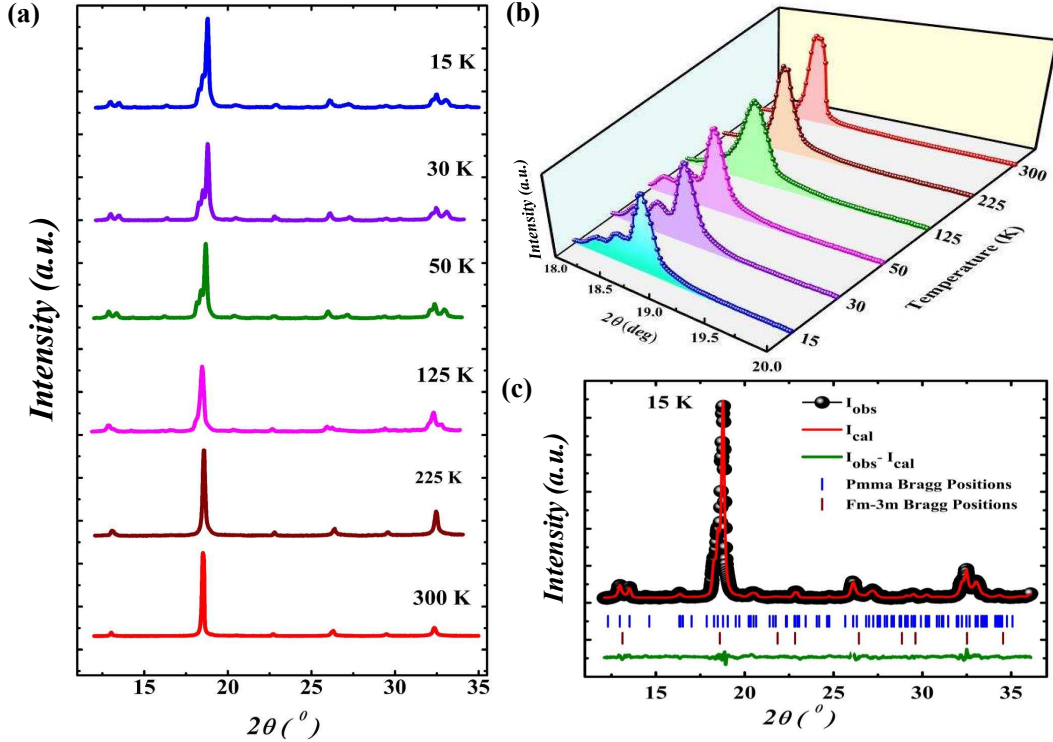


FIG. 7. (a) X-ray diffraction patterns for GdPd₂Bi at various temperatures. (b) Magnified 3-D plot for the most intense peak for various temperatures. (c) X-ray diffraction pattern recorded at 15 K; observed (black circles), calculated (continuous red line), difference (continuous green line) intensities and allowed Bragg positions (blue ticks and brown ticks) are marked in the figure.

TABLE II. Energetics of the different spin configurations of the HT and LT phases of GdPd₂Bi

Phase	Configuration	Gd1	Gd2	Gd3	Gd4	ΔE (meV)
HT	FM	↑	↑	↑	↑	3.77
	AFM	↑	↓	↑	↓	0.0
LT	FM	↑	↑	↑	↑	2.95
	AFM	↑	↓	↑	↓	0.0

with complicated nesting in the BZ. The electron pockets are mostly located around the Γ point, and the hole pockets are at the edge of the BZ near the high symmetry U and X points. Interestingly, although there are some hole pockets in the Fermi surface, the dominant carriers are still in electron pockets in the BZ. The LT case is not exactly same as that of the HT in the context of the carrier pockets in the BZ. In fig. 12(b) insets, the Fermi

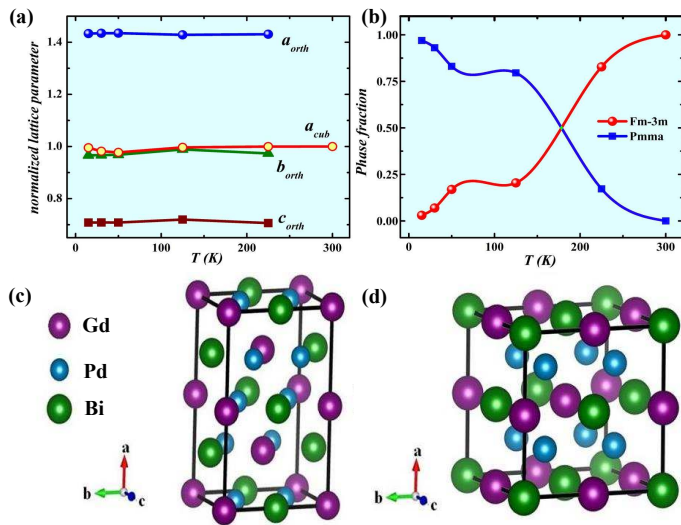


FIG. 8. (a) The thermal variation of lattice parameters (a_{orth} , b_{orth} , c_{orth} and a_{cub}), (b) phase fraction % with temperature. (c) and (d) the crystallographic image of low- T (Pmma) and high- T (Fm $\bar{3}$ m) phase respectively.

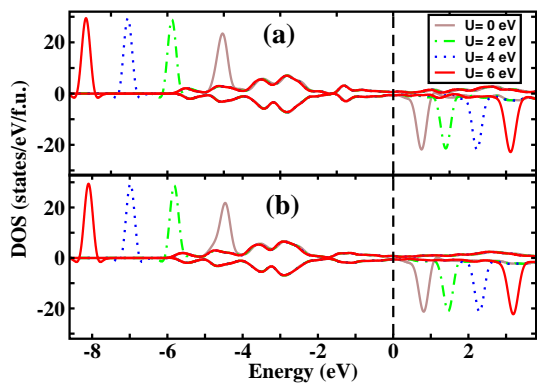


FIG. 9. The calculated spin-polarized DOS for (a) high temperature and (b) low temperature, for different U_{eff} values. Two panels represent majority and minority spin channels for each DOS. The Fermi level is set at zero in the energy scale.

surfaces of the electron and hole pockets are shown for the LT phase, which has few distinct difference compared to that of the HT phase. In the LT phase, the contribution of the electron pocket Fermi surfaces has decreased, whereas- the contribution of the hole pocket Fermi surfaces has increased, compared to that of the HT phase. In fig. 12(b), the hole pockets form two different kind of the Fermi surfaces located around the Γ point and spans larger areas in the BZ. Therefore, from the Fermi surface plots, it is clear that in both HT and LT phases, electrons and holes contribute in the carrier type, however, in the LT phase, the hole contributions have increased compared to that of the HT phase.

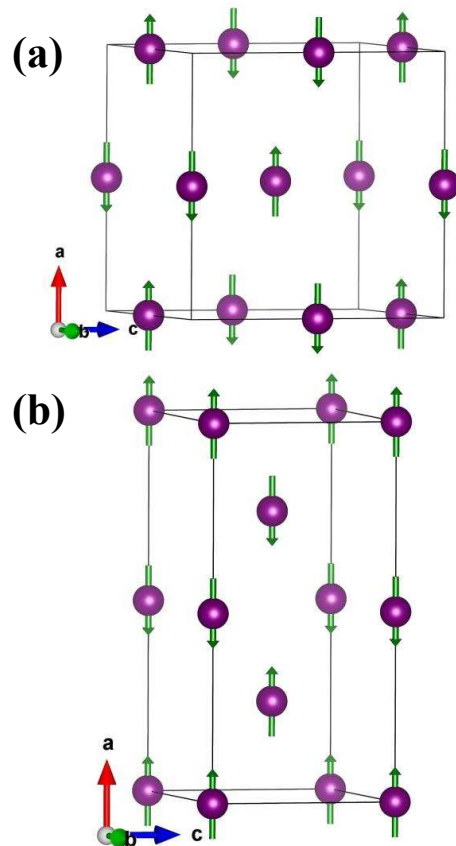


FIG. 10. The pictorial representation of the lowest energy antiferromagnetic spin configurations for (a) HT and (b) LT of GdPd $_2$ Bi in the Gd only sublattice structure.

VI. DISCUSSION

The structural transition from cubic to low-symmetry phase is already reported for REPd $_2$ Bi (RE = Dy and Ho) [13]. However, Gd with orbital angular momentum $L = 0$ at the ground state, is electronically different from the other rare-earth ions. Nevertheless, the observation of structural phase transition indicates that orbital moment has little effect on the phenomenon.

GdPd $_2$ Bi depicts thermal hysteresis in the electrical transport measurement around the structural transition. At high temperatures (> 200 K), the $\rho(T)$ is metallic followed by an upturn below 200 K, and this region of upturn shows thermal hysteresis indicating a first order phase transition. Evidently, this upturn manifests the structural transition observed in our PXRD data [see fig 8]. At lower temperatures below 30 K, the resistivity shows a saturating tendency, which eventually turns metallic under the application of H . Such sharp decrease in ρ under H in the low- T region has also been reported in another half-Heusler compound HoNiSb, which is predominantly semiconducting in nature. In case of HoNiSb, such decrease in $\rho(T)$ in the low temperature, has been attributed to the reduction of spin-disorder scattering

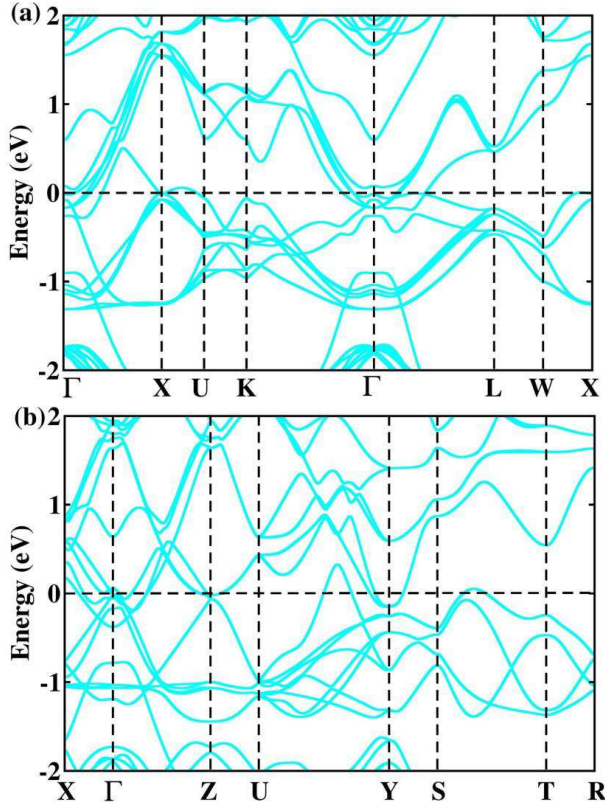


FIG. 11. The calculated spin-polarized GGA+ U +SOC band structures along the high symmetry direction in the Brillouin zone (BZ) for (a) HT and (b) LT of GdPd₂Bi, respectively. The Fermi level is set at zero in the energy scale.

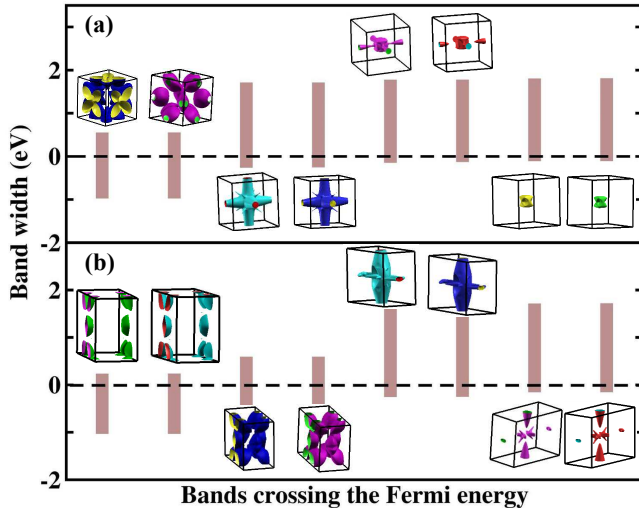


FIG. 12. The calculated GGA+ U +SOC band widths for (a) HT and (b) LT of GdPd₂Bi are indicated by vertical brown bars which crosses the Fermi energy. The corresponding Fermi surfaces are shown in the insets.

due to the alignment of moments under the application of H , and the reduction of the gap occurring due to the splitting of the up and down spin subbands [53]. It is interesting to note that the $\rho(T)$ has remarkable similarities with several transition metal-based shape memory alloys undergoing martensitic phase transition (MPT), where sharp and hysteretic rise in ρ between two metallic phases is observed. The common examples are Ni-Co-Al, Ni-Mn-Sn, Ni-Mn-In etc [22, 24, 25, 50]. In case of one such Ni-Mn-Sn alloys (nominal composition, Ni₂Mn_{1.4}Sn_{0.6}), the rise in ρ around the MPT is about 36%, which is comparable to 43% rise in the presently studied GdPd₂Bi.

The analysis of our T dependent PXRD data indicates that the sample undergoes structural transition from cubic ($Fm\bar{3}m$) to orthorhombic ($Pmma$) structure [see fig 7]. For GdPd₂Bi, we observe robust Bain distortion [50, 54] between cubic and orthorhombic cell parameters: $a_{orth} = \sqrt{2}a_{cub}$, $b_{orth} = a_{cub}$ and $c_{orth} = a_{cub}/\sqrt{2}$. Similar lattice transformation is also observed in case of Co₂NbSn, Ni₂Mn_{1.44}Sn_{0.56} and Ni₂Mn_{1.48}Sb_{0.52} samples across the MPT [51, 52]. For GdPd₂Bi, we observe a 1.5% change in lattice volume across the transition, although the lattice distortion is significant. MPT is a shear-dominated non-diffusive solid to solid phase transition, where the volume change is small [55]. Therefore, the observed transition in GdPd₂Bi is likely to be martensitic-type. The MPT in GdPd₂Bi is clearly first order in nature, which is supported by the phenomenon of phase coexistence obtained from our PXRD data. The further observe thermal hysteresis in our C_P data, which strengthens the first order nature of the MPT.

Another important feature is the occurrence of large negative MR in the title compound. The MR follows an H^2 dependence up to 150 kOe of field and it remains unsaturated. The negative MR is prevalent in the PM phase well above the AFM transition temperature. There are reports of negative MR in several other intermetallic AFM compounds in the PM phase, such as Gd₂PdSi₃, GdSi, GdNi₂Si₂, FeSe₂ [56–59] and so on. For GdNi₂Si₂ negative MR is found both in the PM ($T \gtrsim T_N$) state and also below T_N varying almost quadratically with H . Such behavior, is not attributed to the Kondo effect due to the well-localized character of Gd $4f$ electrons, but rather depends on the spin fluctuations in the Ni $3d$ band [58]. The negative MR close to T_N arises due to the suppression of spin fluctuations by the magnetic field. However, for some compounds (e.g., Gd₂PdSi₃, GdSi), considerable MR exists well above T_N , and it is attributed to the formation of magnetic-polarons. The applied field aligns these magnetic polaron (local FM clusters) leading to the reduction of spin-dependent scattering [57].

From a theoretical point of view, Usami *et al.* [60] studied the MR response of AFM metal in the light of $s-d$ model of electrons. In presence of fluctuating moments from d electrons, the calculation shows a quadratic H dependence of negative MR at low field even in the PM, which eventually saturates at higher fields.

In case of GdPd₂Bi, finite negative MR is observed for

temperature as high as 150 K [see fig. 2(d)] and it is quite unlikely to observe antiferromagnetic fluctuations at temperatures much higher than the T_N . A polaronic picture can be mooted for GdPd₂Bi similar to Gd₂PdSi₃ or GdSi. However, the magnetic susceptibility of GdPd₂Bi shows a perfect Curie-Weiss behavior down to about 15 K, and the data recorded at $H = 100$ Oe and 1 kOe overlap with each other (see lower inset of fig 1). This does not support the picture of spin fluctuations or magnetic polarons, as they would lead to the deviation from the Curie-Weiss law. Additionally, had the MR been related to the spin-fluctuation or magnetic polarons, one would expect a saturation or tendency towards saturation at higher fields. However, we observe a robust H^2 behaviour even at a field as high as 150 kOe. At such a high field, the spin-fluctuation should get completely suppressed or the polarons would have melted. Therefore, a simple spin-fluctuation or polaronic model may not be appropriate here.

GdPd₂Bi shows martensitic transition, and it may contain martensitic variants at low temperature [61]. It has been found (specially in case of ferromagnetic shape memory alloys) that a magnetic field can induce a reverse transition from martensite to austenite leading to negative MR. However, for GdPd₂Bi, we found that the martensitic transition temperature is completely insensitive of H , and therefore, such phenomenon can be ruled out.

A non-saturating positive MR varying quadratically with H is not uncommon. There are several systems having non-trivial topology in their electronic structure, which show nonsaturating positive MR [62–66]. However, the presently studied compound does not belong to that category. Saini *et al.* recently reported quadratically varying positive MR in the single crystal sample of PtAl [67]. The Fermi surface contains both electron and hole pockets similar to the presently studied compound. It appears that the negative MR in GdPd₂Bi does not have a magnetic or structural origin, and it is possibly connected to the complex nature of the Fermi surface.

The most fascinating feature here is the presence of distinct thermal hysteresis in the ρ vs T data both in zero field as well as $H = 100$ kOe. Thermal hysteresis in ρ vs T data is a common feature in the case of Ferromagnetic shape memory alloys (FSMAs) (such as Co–Ni–Al, Ni–Mn–Sn) that undergo a first order phase transition from austenite (cubic) to martensitic (orthorhombic/hexagonal/tetragonal/monoclinic) phase. Interestingly, similar scenario of martensitic phase transformation occurs for GdPd₂Bi.

Further evidence in support of occurrence of first order transition is seen from the C_P and α_S versus T data. A broad anomaly is observed in C_P around 160 K. First order martensitic phase transitions often give rise to an anomaly in C_P , which is of finite width as a result of the system not being in thermal equilibrium [51].

The α_S value for GdPd₂Bi is negative for $T \geq 25$ K and positive below it. Interestingly, the sign of R_H is

negative indicating electrons to be the dominant charge carrier in GdPd₂Bi, which is in line with α_S . However, below about 30 K, the ρ_{xy} turns non-linear indicating the significant contribution of holes in addition to electrons in the system. It might be possible that the contribution from hole carriers becomes significant for $T < 30$ K, which in turn leads to small positive value of α_S . The Fermi surface plot also shows that both HT and LT, two types of carriers i.e. electron and hole exist. However, in the LT phase, the hole contribution as a carrier is more prominent than the HT phase.

VII. SUMMARY AND CONCLUSIONS

An in-depth study of structure, magnetic and electronic ground state of full Heusler GdPd₂Bi compound is presented via x-ray diffraction, magnetization, magnetotransport, thermal transport and heat capacity measurements with further support from DFT calculations. Magnetic study reveal that the compound orders antiferromagnetically at around 7 K. The total energy calculations further confirm that the antiferromagnetic correlation is dominant over the full polarized spin configuration for GdPd₂Bi. Magnetotransport study reveals uncharacteristic thermal hysteresis in 100-200 K range, while no corresponding singularities are observed in the magnetic data. In addition, a fairly high quadratic and nonsaturating magnetoresistance has been observed in this compound. We propose that the negative MR is not directly related to the magnetic properties of the material, rather it arises from the complex nature of the Fermi surface with nesting and electron/hole pockets [68]. Detailed structural analysis reveal a martensitic type structural phase transition is likely to be associated with the thermal hysteresis and no gap opening occurs at E_F for both HT and LT phases. The Hall measurement and electronic structure calculations in presence of SOC corroborate complex character of the electronic structure near Fermi surface due to the presence of both electron and hole bands in poor metallic GdPd₂Bi. SOC is an important parameter in rare-earth based systems which significantly influences physical properties in a system. Tuning the electronic structure can be possible by altering the rare-earth element in REPd₂Bi series. Therefore, our work not only present a thorough study on GdPd₂Bi, but also would boost interest for further investigation on the other members of the REPd₂Bi family.

ACKNOWLEDGMENT

Snehashish Chatterjee, Prabir Dutta and Surasree Sadhukhan would like to acknowledge Univerisity Grants Commission (India), Science and Engineering Research Board (Grant No. PDF/2017/001061), and IIT Goa respectively for their research fellowship. Sudipta Kanungo thanks Department of Science and Technology, Govt. of

India for providing an INSPIRE faculty research grant [Grant No. DST/INSPIRE/04/2016/000431; IFA16-MS91]. UGC DAE-CSR, Indore, and Kolkata Centers are duly acknowledged for low-temperature transport

and heat-capacity measurements. The authors would like to sincerely acknowledge the Indian beamline facility at Photon Factory, KEK, Tsukuba, Japan for low temperature synchrotron x-ray diffraction measurement.

-
- [1] B.R.K. Nanda, I. Dasgupta, J. Phys.: Condens. Matter **15**, 7307 (2003).
- [2] T. Graf, C. Felser, S.S.P. Parkin, Prog. Sol. Stat. Chem. **39**, 1 (2011).
- [3] K. Özdoğan, E. Şaşıoğlu and I. Galanakis, J. Appl. Phys. **113**, 193903 (2013).
- [4] T. Krenke, E. Duman, M. Acet, E.F. Wassermann, X. Moya, L. Mañosa, A. Planes, Nat. Mater. **4**, 450 (2005).
- [5] S. Chatterjee, S. Chatterjee, S. Giri, and S. Majumdar, J. Phys.: Condens. Matter **34**, 013001 (2022).
- [6] M. Ishikawa, J. L. Jorda, and A. Junod, *Superconductivity in d- and f-Band Metals* (Kernforschungszentrum, Karlsruhe), 1982 p. 141.
- [7] M. J. Johnson and R. N. Shelton, Solid State Commun. **52**, 839 (1984).
- [8] S.K. Malik, A.M. Umarji, and G.K. Shenoy Phys. Rev. B **31**, 11 (1985).
- [9] H. Lin, L. A. Wray, Y. Xia, S. Xu, S. Jia, R. J. Cava, A. Bansil and M. Z. Hasan, Nature Mat. **9**, 546 (2010).
- [10] W. Al-Sawai, Hsin Lin, R. S. Markiewicz, L. A. Wray, Y. Xia, S.-Y. Xu, M. Z. Hasan, and A. Bansil, Phys. Rev. B **82**, 125208 (2010).
- [11] C. Shekhar, S. Ouardi, A. K. Nayak, G. H. Fecher, W. Schnelle, and C. Felser, Phys. Rev. B **86**, (2012) 155314.
- [12] C. Shekhar, N. Kumar, V. Grinenko, S. Singh, R. Sarkar, H. Luetkens, S.-C. Wu, Y. Zhang, A. C. Komarek, E. Kampert, Y. Skourski, J. Wosnitza, W. Schnelle, A. McCollam, U. Zeitler, J. Kübler, B. Yan, H.-H. Klauss, S. S. P. Parkin, and C. Felser, Proc. Natl. Acad. Sci. U. S. A. **115**(37), 9140 (2018).
- [13] K. Gofryk, D. Kaczorowski, T. Plackowski, A. Leithe-Jasper and Yu. Grin, Phys. Rev. B **72**, (2005) 094409.
- [14] K. Gofryk, ‘*Thermoelectric properties 4f and 5f-Heusler electronic phases $RPdX$ and RPd_2X ($X = Sb$ and Bi)*’, Institute of Low Temperature and Structure Research, Polish Academy of Sciences, Wrocław, Poland (2005).
- [15] <http://maud.radiographema.eu>.
- [16] G. Kresse and J. Hafner, Phys. Rev. B **47**, 558(R) (1993).
- [17] G. Kresse and J. Furthmüller, Phys. Rev. B **54**, 11169 (1996).
- [18] J. P. Perdew, K. Burke, and M. Ernzerhof, Phys. Rev. Lett. **77**, 3865 (1996).
- [19] V. I. Anisimov, I. V. Solovyev, M. A. Korotin, M. T. Czyzyk, and G. A. Sawatzky, Phys. Rev. B **48**, 16929 (1993).
- [20] S. L. Dudarev, G. A. Botton, S. Y. Savrasov, C. J. Humphreys, and A. P. Sutton, Phys. Rev. B **57**, 1505 (1998).
- [21] S. Chatterjee, P. Dutta, S. Giri, S. Majumdar, S. Sadhukhan, S. Kanungo, S. Chatterjee, M. M. Patidar, G. S. Okram and V. Ganesan, Phys. Rev. B **102**, 214443 (2020).
- [22] P. J. Brown, A. P. Gandy, R. Kainuma, T. Kanomata, K. U. Neumann, K. Oikawa, B. Ouladdiaf, A. Sheikh and K. R. A. Ziebeck, J. Phys.: Condens. Matter **23**, 456004 (2011).
- [23] S. Chatterjee, S. Giri, S. Majumdar, and S. K. De Phys. Rev. B **77**, 012404 (2008).
- [24] S. Chatterjee, S. Giri, S. Majumdar, and S. K. De Phys. Rev. B **77**, 224440 (2008).
- [25] S. Chatterjee, M. Thakur, S. Giri, S. Majumdar, A.K. Deb, S.K. De, J. Alloys Compound, **456**, 96 (2008).
- [26] M. Kohler, Ann. Phys. (Berlin) **424**, 211 (1938).
- [27] K. K. Kolincio, M. Roman and T. Klimczuk Phys. Rev. Lett. **125**, 176601 (2020).
- [28] C. Candolfi, A. Ormeci, U. Aydemir, M. Baitinger, N. Oeschler, Yu. Grin, and F. Steglich Phys. Rev. B **84**, 205118 (2011).
- [29] A. Wang, D. Graf, Y. Liu, Q. Du, J. Zheng, H. Lei and C. Petrovic Phys. Rev. B **96**, 121107(R) (2017).
- [30] K. A. Gschneidner, Jr. and V. K. Pecharsky, J. Rare Earths **24**, 641 (2006).
- [31] H. Goldsmid, *Thermoelectric Refrigeration* (Temple Press Books Ltd., London) (1964).
- [32] D. Kaczorowski, K. Gofryk, T. Plackowski, A. Leithe-Jasper and Yu. Grin, J. Mag. Mag. Mater **290**, 573 (2005).
- [33] K. Gofryk, D. Kaczorowski, T. Plackowski, A. Leithe-Jasper, and Yu. Grin Phys. Rev. B **84**, 035208 (2011).
- [34] H. Hohl, A. P. Ramirez, W. Kaefer, K. Fess, C. Thurner, C. Kloc, and E. Bucher, MRS Proc. **478**, 109 (1997).
- [35] H. Zhu, R. He, J. Mao, Q. Zhu, C. Li, J. Sun, W. Ren, Y. Wang, Z. Liu, and Z. Tang et al., Nat. Commun. **9**, 1 (2018).
- [36] D. Young, P. Khalifah, R. Cava, and A. Ramirez, J. Appl. Phys. **87**, 317 (2000).
- [37] H.-S. Kim, Z. M. Gibbs, Y. Tang, H. Wang, and G. J. Snyder, APL Mater. **3**, 041506 (2015).
- [38] C.S. Lue, C.F. Chen, J.Y. Lin, Y.T. Yu, Y.K. Kuo, Phys. Rev. B **75**, 064204 (2007).
- [39] C.S. Lue, J.W. Huang, D.S. Tsai, K.M. Sivakumar, Y.K. Kuo, J. Phys. Condens. Matter **20** 255233 (2008).
- [40] A. C. Melissinos, *Experiments in Modern Physics* (Academic Press, An Imprint of Elsevier, California), pp. 86 (1966).
- [41] S. U. Jen, B. L. Chao, and C. C. Liu. J. Appl. Phys. **76**, 5782 (1994).
- [42] A. Laha, R. Singha, S. Mardanya, B. Singh, A. Agarwal, P. Mandal and Z. Hossain, Phys. Rev. B **103**, L241112 (2021).
- [43] J. Honig and T. Harman, Adv. Energy Convers. **3**, 529 (1963).
- [44] G. Pokharel, S. M. L. Teicher, B. R. Ortiz, P. M. Sarte, G. Wu, S. Peng, J. He, R. Seshadri and S. D. Wilson, Phys. Rev. B **104**, 235139 (2021).
- [45] Y. Yang, Y. Fu, W. Zhu, J. He, B. Liu, C. B. Liu, L. Li, C. Niu and Y. Luo, J. Phys.: Condens. Matter **34** 315701 (2022).
- [46] F. G. Aliev, Physica B **171**, 199 (1991).

- [47] I. M. Tsidilkovski, *Electron Spectrum of Gapless Semiconductors*, Springer Series in Solid-State Sciences **116** Springer, Berlin, New York, (1996).
- [48] H. T. Stokes, D. M. Hatch, and B. J. Campbell, ISODIS-TORT, ISOTROPY Software Suite, *iso.byu.edu*.
- [49] B. J. Campbell, H. T. Stokes, D. E. Tanner, and D. M. Hatch, *J. Appl. Cryst.* **39**, 607 (2006).
- [50] P. J. Brown, A. P. Gandy, K. Ishida, R. Kainuma, T. Kanomata, K-U Neumann, K. Oikawa, B. Ouladdiaf and K. R. A. Ziebeck, *J. Phys.: Condens. Matter* **18**, 2249 (2006).
- [51] K-U Neumann, T. Kanomata, B. Ouladdiaf and K. R. A. Ziebeck, *J. Phys.: Condens. Matter* **14**, 1371 (2002).
- [52] J. Sannigrahi, S. Pramanick, S. Chatterjee, J. S. Lord, D. Khalyavin, A. D. Hillier, D. T. Adroja, and S. Majumdar *Phys. Rev. B* **99**, 224401 (2019).
- [53] I. Karla, J. Pierre and R.V. Skolozdra, *J. Alloys Compound* **265**, 42 (1998).
- [54] Sanjay Singh, B. Dutta, S.W. D'Souza, M.G. Zavareh, P. Devi, A.S. Gibbs, T. Hickel, S. Chadov, C. Felser and D. Pandey, *Nat Commun* **8**, 1006 (2017).
- [55] V A Chernenko *Scr. Mater.* **40**, 523 (1999).
- [56] R. Mallik *et al* *E. Phys. Lett.* **41**, 315 (1998).
- [57] H. Li, Y. Xiao, B. Schmitz, J. Persson, W. Schmidt, P. Meuffels, G. Roth and T. Brückel *Sci Rep* **2**, 750 (2012).
- [58] E. V. Sampathkumaran and I. Das, *Phys. Rev. B* **51**, 8631 (1995).
- [59] H. Liu and Y. Xue *Adv. Mater.* **33**, 2008456 (2021).
- [60] K. Usami, *J. Phys. Soc. Jpn* **45**, 466 (1978).
- [61] B. Kiefer, and D. C. Lagoudas, *Phil. Mag.* **85**, 4289 (2005)
- [62] M. Ali, J. Xiong, S. Flynn *et al.* *Nature* **514**, 205 (2014).
- [63] C. Shekhar, A. Nayak, Y. Sun *et al.* *Nature Phys* **11**, 645–649 (2015).
- [64] B. Wu, V. Barrena, F. Mompeän, M. G.-Hernández, H. Suderow, and I. Guillamón *Phys. Rev. B* **101**, 205123 (2020).
- [65] Z. Li, Y. Zeng, J. Zhang, M. Zhou, and W. Wu *Phys. Rev. B* **98**, 165441 (2018).
- [66] Y. Li, L. Li, J. Wang, T. Wang, X. Xu, C. Xi, C. Cao, and J. Dai *Rev. B* **94**, 121115(R) (2016).
- [67] V. Saini, S. Sasmal, R. Kulkarni, B. Singh, and A. Thamizhavel *Phys. Rev. B* **106**, 125126 (2022).
- [68] O. Breunig, Z. Wang, A. A. Taskin, J. Lux, A. Rosch and Y. Ando *Nat. Commun.* **8**, 15545 (2017).